Izvestiya. Non-Ferrous Metallurgy • 2024 • Vol. 30 • No. 2 • P. 70–84

CORROSION AND PROTECTION OF METALS / КОРРОЗИЯ И ЗАЩИТА МЕТАЛЛОВ

UDC 669.717: 669.718: 621.9.048
https://doi.org/10.17073/0021-3438-2024-2-70-84

Research article
Научная статья

Influence of manganese alloying on the structure and properties of electrospark coatings of EP741NP heat-resistant nickel LPBF alloy

S.K. Mukanov, M.I. Petrzhik, P.A. Loginov, E.A. Levashov

National University of Science and Technology "MISIS"
4 Bld. 1 Leninskiy Prosp., Moscow 119049, Russia

✉ Samat K. Mukanov (smukanov@misis.ru)

Abstract: The paper investigates the impact of Mn content (Mn = 0; 0.5; 0.6; 1; 1.5 at.%) in the composition of the electrodes of the Al–Ca–Mn system on the structure and properties of electrospark coatings formed on LPBF substrates made of EP741NP alloy. It was found that the highest weight gain of the substrate ($5.8 \cdot 10^{-4}$ g) was recorded when the Al–7%Ca–1%Mn electrode with a low degree of supercooling of the melt ($\Delta t = 5$ °C) was subject to electrospark treatment (EST). EST with this electrode with a fine eutectic structure enables the formation of coatings with minimal surface roughness ($R_a = 3.51 \pm 0.14$ μm). The nanocrystalline structure of the coatings was confirmed by transmission electron microscopy, including HRTEM. Comparative tribological tests revealed that the coating with maximum hardness (10.7±0.8 GPa) formed during EST with an electrode containing 1.5 at.% Mn had the minimal wear rate ($1.86 \cdot 10^{-5}$ mm^3/(N·m)). We proved that EST with Al–Ca–Mn electrodes enables to reduce the specific weight gain of the LPBF EP741NP alloy during isothermal ($t = 1000$ °C) curing in air due to *in situ* formation of a complex thermal barrier layer consisting of oxides (α-Al_2O_3, $CaMoO_4$) and intermetallides (γ'-Ni_3Al and β-NiAl). We determined the concentration limit of Mn (1.0 at.%) in the electrode, at which the barrier layer retains its integrity and functionality.

Keywords: heat-resistant nickel alloy, laser powder bed fusion (LPBF), electrospark treatment, wear resistance, oxidation resistance, thermal barrier layer.

Acknowledgments: This work was funded by the Ministry of Science and Higher Education of the Russian Federation under state research assignment (project No. 0718-2020-0034).

For citation: Mukanov S.K., Petrzhik M.I., Loginov P.A., Levashov E.A. Influence of manganese alloying on the structure and properties of electrospark coatings of EP741NP heat-resistant nickel LPBF alloy. *Izvestiya. Non-Ferrous Metallurgy.* 2024;30(2):70–84.
https://doi.org/10.17073/0021-3438-2024-2-70–84

Влияние легирования марганцем на структуру и свойства электроискровых покрытий на никелевом жаропрочном СЛС-сплаве ЭП741НП

С.К. Муканов, М.И. Петржик, П.А. Логинов, Е.А. Левашов

Национальный исследовательский технологический университет «МИСИС»
Россия, 119049, г. Москва, Ленинский пр-т, 4, стр. 1

✉ Самат Куандыкович Муканов (smukanov@misis.ru)

Аннотация: Исследовано влияние содержания марганца (Mn = 0; 0,5; 0,6; 1; 1,5 ат.%) в составе электродов системы Al–Ca–Mn на структуру и свойства электроискровых покрытий, сформированных на СЛС-подложках из сплава ЭП741НП. Обнаружено, что наибольший привес массы подложки ($5{,}8\cdot10^{-4}$ г) зафиксирован при электроискровой обработке (ЭИО) электродом Al–7%Ca–1%Mn, имеющим низкую степень переохлаждения расплава (Δt = 5 °C). Процесс ЭИО данным электродом с тонкой эвтектической структурой позволяет формировать покрытия с минимальной шероховатостью поверхности (R_a = 3,51±0,14 мкм). Нанокристаллическая структура покрытий была подтверждена методами просвечивающей электронной микроскопии, в том числе с высоким разрешением. По результатам сравнительных трибологических испытаний обнаружено, что наилучшей износостойкостью ($1{,}86\cdot10^{-5}$·мм^3/(Н·м)) обладает покрытие с максимальной твердостью (10,7±0,8 ГПа), сформированное в процессе ЭИО электродом с содержанием 1,5 ат.% Mn. Показано, что ЭИО электродами Al–Ca–Mn позволяет снизить удельный привес СЛС-сплава ЭП741НП при изотермической (t = 1000 °C) выдержке на воздухе благодаря *in situ* формированию комплексного термобарьерного слоя, состоящего из оксидов (α-Al_2O_3, $CaMoO_4$) и интерметаллидов (γ'-Ni_3Al, β-NiAl) . Установлен предел концентрации Mn (1,0 ат.%) в электроде, при которой барьерный слой сохраняет свои целостность и функциональность.

Ключевые слова: жаропрочный никелевый сплав, селективное лазерное сплавление, электроискровая обработка, износостойкость, стойкость к окислению, термобарьерный слой.

Благодарности: Работа выполнена при финансовой поддержке Министерства науки и высшего образования РФ в рамках государственного задания (проект 0718-2020-0034).

Для цитирования: Муканов С.К., Петржик М.И., Логинов П.А., Левашов Е.А. Влияние легирования марганцем на структуру и свойства электроискровых покрытий на никелевом жаропрочном СЛС-сплаве ЭП741НП. *Известия вузов. Цветная металлургия.* 2024;30(2):70–84. https://doi.org/10.17073/0021-3438-2024-2-70–84

Introduction

Gas turbine components play a key role in the operation of power generators [1; 2]. Nowadays, steam pressure is increased to 35 MPa and temperature — to 750 °C [3] (there are plans to raise it to 1000 °C in the future) to enhance efficiency and environmental protection in the working zone of power plants. For this reason, gas turbine blades [3] are made of nickel-based heat-resistant alloys (Inconel, GTD, MGA, etc.) that can function under severe conditions of high temperatures and centrifugal loads. The structure of classical nickel superalloys includes the face-centered cubic (FCC) matrix and strengthening γ'-phases [5]. Reasonable alloying of such a structure ensures excellent mechanical properties and creep resistance at elevated temperatures up to 1150 °C [6; 7].

However, temperature and vibration gradients, as well as the ingress of various kinds of abrasive into the working zone can lead to critical wear and premature turbine failure [8—10]. Therefore, improving the wear resistance of nickel superalloy parts is crucial for ensuring the reliability and durability of gas turbine blades. Various methods of deposition of coatings and/or modification of surfaces of item are used to achieve this objective. Deposition/synthesis of refractory phases (NiAl intermetallides, NiB borides [11], and Al_2O_3, Y_2O_3, ZrO_2 oxides [6; 12]) responsible for wear and oxidation resistance of coatings in various gas environments at elevated temperatures are used to prevent premature wear. One traditional method of surface hardening is plasma spraying of Tribaloy T-800 coatings [13] coatings onto the contact surface of casings. These coatings are based on a Co—Cr—Mo alloy system and structurally reinforced with Laves phases. However, such coatings are unstable due to difference in thermal expansion coefficients of the microstructural constituents, which leads to cracks generation.

In addition, there is an issue of mutual diffusion of alloying elements at the interface between the coating and superalloy at high temperatures. It is solved by using thermal barrier coatings with increased oxidation resistance. They typically consist of an outer ceramic layer containing a basic oxide (ZrO_2 or Al_2O_3) stabilized with yttrium (6—9 wt.% Y_2O_3) so called YSZ [14] and are characterized with a porosity of 10—25 % and a low thermal conductivity (1.5—3.0 $W\cdot m^{-1}\cdot K^{-1}$) [15]. Modern thermal barrier coatings [16] have a gradient microstructure in which each layer is obtained using different techniques.

The technique of electron-beam deposition of thermal barrier coatings is used to extend the service life of parts and assemblies made of superalloys. It also has its disadvantages due to low adhesion of the coating to the substrate [17].

The surface also can be protected from wear and oxidation by means of electrospark treatment (EST) with fusible Al–based electrodes. It is due to in-situ reaction finished by synthesis of intermetallides. This was found in [18] when Al—Si, Al—Ca—Si, Al—Ca—Mn electrodes were used for EST of EP741NP alloy obtained by laser powder bed fusion (LPBF). It was shown that during EST with these electrodes NiAl, Ni_3Al, $NiAl_3$ hard intermetallics have been formed, increasing the wear resistance of EP741NP alloy by 4.5 times. In addition, the coating formed by the Al—Ca—Mn electrode showed excellent resistance to oxidation in air at t = 870 °C, as dense and homogeneous $CaAl_2O_4$ barrier layer was formed and the proportion of β-NiAl increased. When the annealing temperature reached 1000 °C for 30 h, the investigated coating was found to change the oxidation kinetics from a linear law which is typical for SLM superalloy to a parabolic law. This effect is caused by the formation of a two-layer Al_2O_3 /$CaMoO_4$ protective barrier on the surface, which reduces the oxidation rate by 16 times.

When manganese has been added to aluminum alloys it leads to a positive impact on their mechanical properties and heat resistance. However, as its content exceeds 1.5 wt.%, coarse inclusions of the Al_xMn phase in microstructure are released, significantly deteriorating casting properties [19; 20]. Therefore, it is extremely important to investigate the influence of Mn in composition of the electrode on the properties of electrospark coatings.

The purpose of the work was to study how Mn content within the Al—Ca—Mn electrode affects the structure and properties of coatings formed by electrospark treatment of SLM substrates made of EP741NP alloy.

Materials and methods

As substrates we used parallelepiped-shaped samples with the size of 4 × 5 × 15 mm obtained by laser powder bed fusion from EP741NP alloy of the following composition, at.%:

Ni	55.38	Nb	1.62
Co	15.49	C	0.19
Al	10.84	Hf	0.08
Cr	10.03	B	0.08
Mo	2.29	Mg	0.05
Ti	2.18	Cr	0.017
W	1.75	Ce	0.003

Electrospark treatment of the nickel alloy additive surfaces was performed at the rotary motion of the electrode according to the scheme “electrode — cathode, substrate — anode” in the argon medium (99.998 %) at constant values of frequency, duration and pulse energy: 1920 Hz, 25 μs and 48 mJ, respectively.

The composition of near-eutectic electrodes was chosen based on the analysis of the Al—Ca—Mn phase diagram [20]. The charge was melted in an electric furnace GF1100N2D (Graficarbo, Italy) using high purity materials (A99; Ca 99.99) and addition alloy Al—20 wt.% Mn. Core electrodes with a diameter of 3—4 mm, the composition of which is presented in Table 1, were prepared by sucking the melt into a quartz tube.

The kinetics of mass transfer during EST was investigated by the gravimetric method on a KERN 770 precision balance (Germany) with an accuracy of 10^{-5} g. Differential scanning calorimetry (DSC) at a rate of 20 °K/min in a protective argon atmosphere was performed according to the scheme 25—700—25 (°C) on a DSC 404 C Pegasus calorimeter (“Netzsch”, Germany).

The microstructure and composition were studied on a S-3400N scanning electron microscope (“Hitachi”, Japan) equipped with a NORAN System 7 *X*-ray Microanalysis System spectrometer (“Thermo Scientific”, USA). The fine structure was analyzed using a JEM-2100 transmission electron microscope (TEM) (Jeol, Japan). The samples (lamellae) for TEM were cut by the focused ion beam (FIB) method on a Quanta 200 3D FIB instrument (“FEI Company”, USA). The X-ray diffraction (XRD) phase analysis was performed based on the spectra obtained on an automated DRON-4 diffractometer (“Burevestnik”, Russia) using monochromatic CoK_α-radiation in the range of angles 2θ from 10° to 130°.

Comparative tribological tests were performed using a reciprocating movement according to the “rod—plate” scheme on an automated Tribometer friction machine (“CSM Instruments”, Switzerland) in compliance with ASTM G 99-17 at room temperature. The ball with a diameter of 3 mm made of 100Cr6 steel (analog of ShKh15) was used as a counterbody. The following test conditions were met: the track length was 4 mm, the applied load was 2 N, and maximum speed was 5 cm/s. Surface roughness and wear track profiles were studied on a WYKO NT1100 optical profilometer (“Veeco”, USA). Mechanical properties (hardness and elastic modulus) were investigated on a Nano—HardnessTester (“CSM Instruments”, Switzerland) at a maximum load of 10 mN.

The resistance to high-temperature oxidation of electrospark coatings was evaluated by the sample weight gain after isothermal annealing at 1000 °C for

Table 1. **Composition of rod electrodes of the Al—Ca—Mn system**

Таблица 1. Состав стержневых электродов системы Al—Ca—Mn

Designation	Concentration of elements, at.%		
	Al	Ca	Mn
Al—5Ca	94.82	5.18	–
Al—7.5Ca—0.5Mn	92.00	7.5	0.50
Al—5.7Ca—0.6Mn	93.68	5.71	0.61
Al—7Ca—1Mn	92.00	7.00	1.00
Al—6.5Ca—1.5Mn	92.00	6.50	1.50

30 h in air. Oxidation annealing of the samples was conducted in a SNOL 7.2/1200 muffle electric furnace. After annealing with a duration of 0.25, 0.5, 0.75, 1, 2, 3, 4, 5 and then every 5 h samples were weighed at room temperature on ALC-210d4 Acculab analytical scales (USA) with an accuracy of 10^{-5} g. Specific weight gain was calculated according to the formula

$$K = \Delta m / S_0, \qquad (1)$$

where Δm is the difference between the masses of the sample before the test and after oxidation, mg; S_0 is the total surface area of the sample before the test, cm^2.

Results and discussion

The rod electrodes were studied using the DSC method (Fig. 1) to determine the temperatures of melting (t_M) and solidification (t_S). Melting proceeds in a single endothermal peak for all compositions, and when alloys containing more than 6.5 at.% Ca solidify, small exothermic effects associated with the precipitation of $Al_{10}CaMn_2$ primary crystals from the melt are noticeable at temperatures higher than the main solidification exopeak.

The microstructure of quenched electrodes is highly dependent on the material composition. Fig. 1 and Table 2 demonstrate that Mn addition to the Al—Ca base electrode correlates with the formation of primary Al_4Ca crystals (Fig. 2). Solidification of the Al—5%Ca electrode starts with the formation of Al dendrites, 20—30 μm in size, around which a double eutectic with a composition of $Al_{94}Ca_6$ crystallizes. Other electrode (Al—5.7%Ca—0.6%Mn) alloyed with manganese, solidifies with the formation of primary Al_4Ca crystals in the form of plates of the same size, as well as the $Al_{10}CaMn_2$ phase and triple eutectics $Al_{94.1}Ca_{5.3}Mn_{0.6}$.

The microstructure of the Al—7.5Ca—0.5Mn electrode with the increased calcium content also contains primary Al_4Ca crystals in the form of plates, but their portion is higher, while the composition of the ternary eutectic is the same — $Al_{94.2}Ca_{5.2}Mn_{0.6}$. Comparing the compositions of electrodes and eutectics, we can conclude that manganese is not found in the primary crystals of the Al—7.5Ca—0.5Mn electrode and is part of eutectic. The microstructure of the Al—7Ca—1Mn electrode contains plates of primary Al_4Ca crystals, $Al_{10}CaMn_2$ particles, and eutectic with a composition of $Al_{94.3}Ca_{5.3}Mn_{0.4}$. The Al—6.5Ca—1.5Mn electrode has the same microstructure, only with a higher volume

Table 2. **Composition and DSC results of Al–Ca–Mn electrodes**

Таблица 2. Состав и результаты ДСК электродов Al–Ca–Mn

Electrode	t_M, °C	t_S, °C	$\Delta t = t_M - t_S$, °C
Al–5Ca	622	609	13
Al–5.7Ca–0.6Mn	620	607	13
Al–7.5Ca–0.5Mn	619	612	7
Al–7Ca–1Mn	616	611	5
Al–6.5Ca–1.5Mn	617	606	11

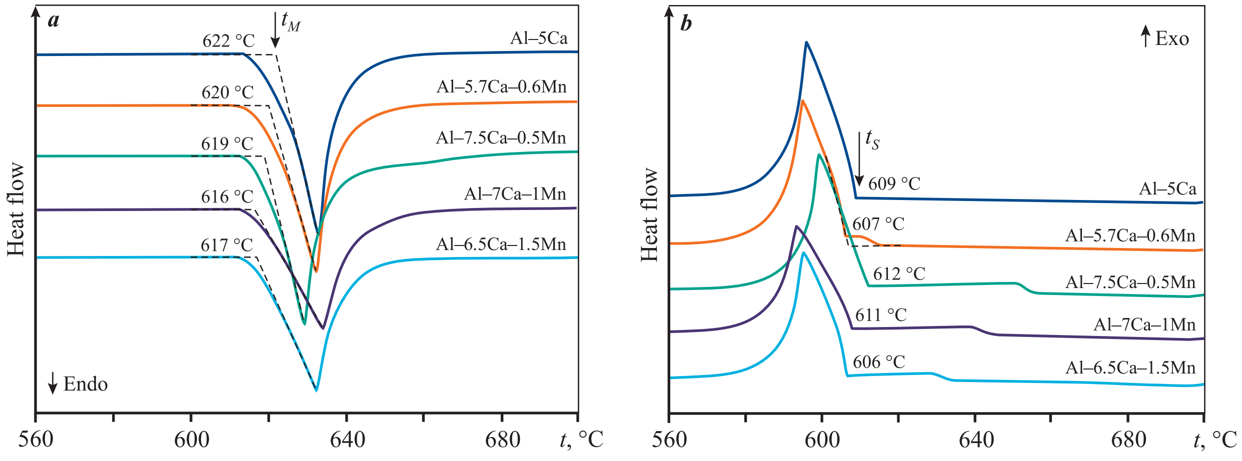

Fig. 1. Thermograms of Al–Ca–Mn rod electrodes
a – melting curves, ***b*** – solidification curves

Рис. 1. Термограммы стержневых электродов Al–Ca–Mn
a – кривые плавления, ***b*** – кривые затвердевания

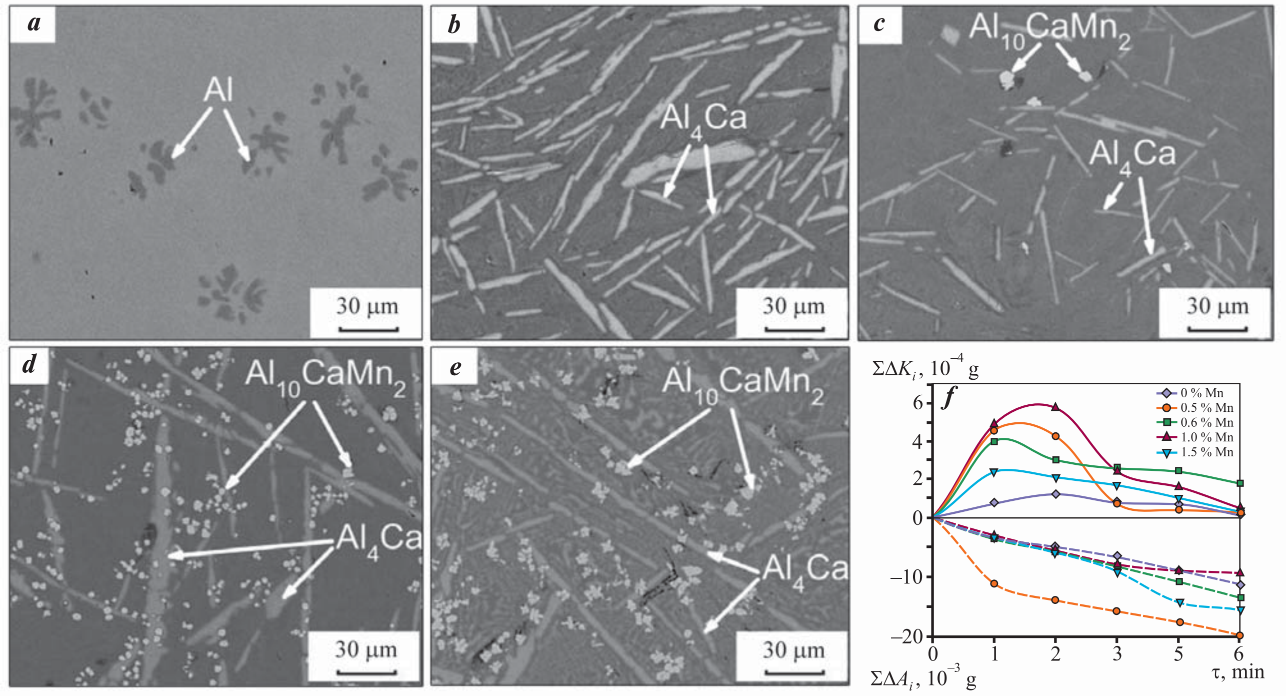

Fig. 2. SEM images of the electrode structure Al–5Ca (***a***), Al–7.5Ca–0.5Mn (***b***), Al–5.7Ca–0.6Mn (***c***), Al–7Ca–1Mn (***d***), Al–6.5Ca–1.5Mn (***e***) and kinetic curves of electrode mass transfer on Ni substrate (***f***)

Рис. 2. РЭМ-изображения структуры электродов Al–5Ca (***a***), Al–7,5Ca–0,5Mn (***b***), Al–5,7Ca–0,6Mn (***c***), Al–7Ca–1Mn (***d***), Al–6,5Ca–1,5Mn (***e***), кинетические кривые массопереноса электродов на Ni-подложку (***f***)

fraction of $Al_{10}CaMn_2$ particles and coarser ternary eutectic.

The kinetic curves of mass transfer during EST of EP741NP alloy with electrodes with different Mn content are presented in Fig. 2, *f*. All of them are of an extreme nature. The highest substrate weight gain ($\Delta K = 5.8 \cdot 10^{-4}$ g) was recorded after 2 minutes of treatment using the near-eutectic Al—7Ca—1Mn electrode that contains small $Al_{10}CaMn_2$ particles in its microstructure (see Fig. 2, *d*) and has a low degree of supercooling ($\Delta t = 5$ °C) (see Table 2). The electrode erosion (ΔA) is slightly higher (Fig. 2, *f*) than the cathode weight gain (ΔK). There is no clear correlation between these parameters, which indicates a significant dispersion of erosion products (molten metal) in the interelectrode gap.

Figure 3 presents images of the microstructure of electrospark coatings on cross sections. The coatings formed during EST with electrodes, their Mn content (at.%) amounting to 0, 0.5, and 0.6, consist of submicron spherical particles. Near the coating surface, their size is less than 1 μm and it increases towards the substrate (Fig. 3, *a*—*c*). The submicron structure of the electrospark layers indicates that after local melting when exposed to electric discharges, the melt cooling rate reaches 10^5—10^6 K/s [21].

The thickness of the investigated electrospark coatings depends on the electrode composition and varies from 11 to 22 μm. After treatment with an electrode containing 1.5 at.% Mn (Fig. 3, *d*), the coating has a layered structure. The near-surface layer of this sample, as well as other ones (Fig. 3, *a*—*c*), consists of well-connected particles smaller than 1 μm. The bottom layer, however, is formed of columnar crystals oriented along the direction of heat removal. The ratio of Ni to Al in the electrospark coating varies with depth: closer to the surface, Al content is higher and as the substrate nears, the amount of Ni increases. According to the EDS data, the highest Mn concentrations (0.9—1.0 at.%) along with Ca (3.4—3.9 at.%) were found in the dark coating areas, whereas the light areas correspond to β-NiAl.

Figure 4 shows the structural constituents of the coating formed during EST with the Al—7%Ca—1%Mn fusible electrode. Its thickness, as well as that of the coating formed with the Al—7.5Ca—0.5Mn electrode (Fig. 3, *c*), is within ~15 μm, and the microstructure includes the regions (Fig. 4, *a*, zone *I*) formed as a result of concentration stratification of the melt. This structure feature is characteristic of the coatings formed by the electrodes with low degree of supercooling — Al—7.5Ca—0.5Mn (7 °C) and Al—7Ca—1Mn (5 °C).

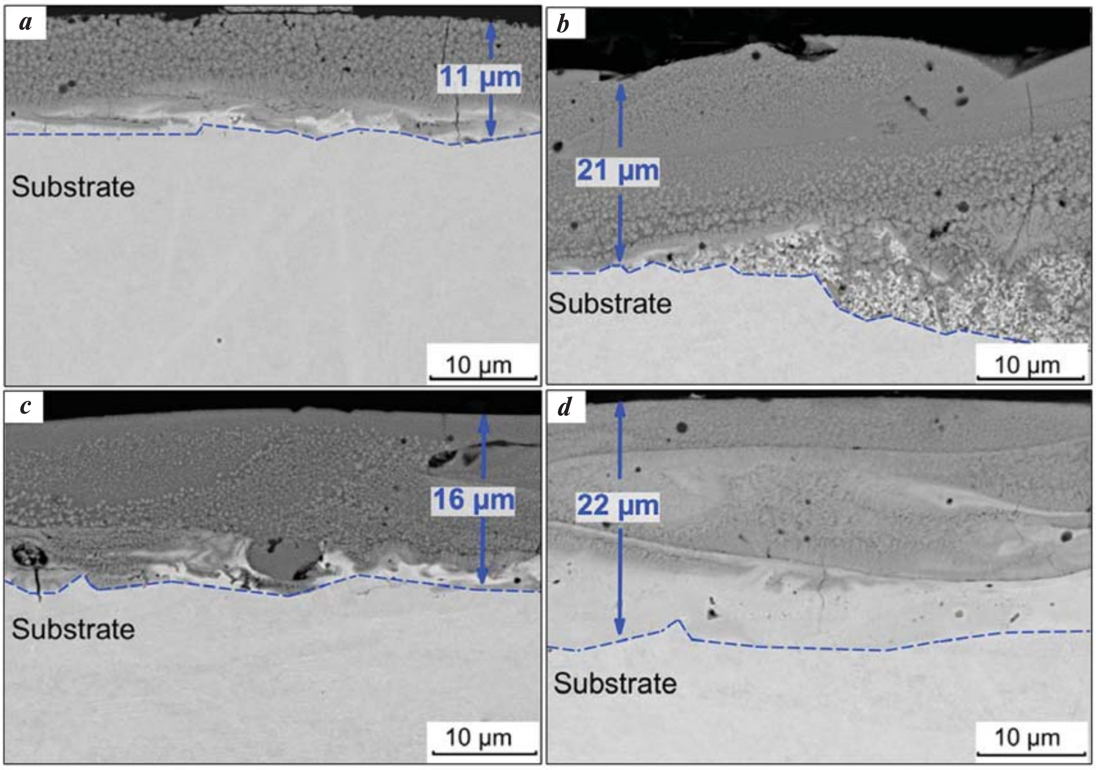

Fig. 3. SEM images of the microstructure of electrospark coatings obtained during EST with electrodes Al–5Ca (***a***), Al–5.7Ca–0.6Mn (***b***), Al–7.5Ca–0.5Mn (***c***) and Al–6.5Ca–1.5Mn (***d***)

Рис. 3. РЭМ-изображения микроструктуры электроискровых покрытий, полученных при ЭИО электродами Al–5Ca (***a***), Al–5,7Ca–0,6Mn (***b***), Al–7,5Ca–0,5Mn (***c***) и Al–6,5Ca–1,5Mn (***d***)

Figure 4, *b* shows that the electrode made of Al—7Ca—1Mn alloy is used to form a coating with a layered structure, which can be divided into two characteristic zones. Zone *I* consists of crystallites with a transverse grain size of 1.0—1.5 μm. Fig. 4, *c* demonstrates that the grains contain spherical nanoscale particles distributed in interlayers (indicated by white arrows). The average thickness of interlayers (strips) in which nanoparticles are found is less than 10 nm. According to the EDS data, their elemental composition does not differ from that of the matrix and they possibly represent shear strips. These interlayers are mostly oriented along the direction of heat removal (perpendicular to the substrate). The HRTEM image (inset *A*) shows that the particles have a diameter of about ~20 nm. The Fourier transform of the particles' images along the zone axis [011] (Fig. 4, inset *B*) revealed that the particles are isostructural to calcium oxide CaO.

In zone *II*, the grains are ~3.5 μm long and have an elongated shape. The direction of the columnar crystallite growth coincides with that of heat removal. Increased concentrations of Al (53.2 at.%), Ca (1.4 at.%) and Mn (0.5 at.%) are observed in this region, but Ni content shrinks (28.3 at.%). According to the TEM diffraction pattern in region II (insert C), the values of interplane distances (1.99 nm and 2.82 nm) correspond to Ni_2Al_3 trigonal syngony with the $P\bar{3}m1$ space group.

According to the linear EDS analysis data obtained in the mode of scanning transmission electron microscope, the particles are enriched with calcium (Fig. 5), while the concentrations of all other elements (Al, Ni, Co, Cr) sharply drop. The Ca content reaches 30 at.% and that of oxygen — 19.4 at.%. This is consistent with the HRTEM findings (Fig. 4, inset *B*) indicating that the particles are a complex oxide of the (CaMe)O type. The formation of these particles during EST may be attributed to the reduction of metal oxides by calcium, which has a high affinity for oxygen [22].

Figure 6 shows that manganese alloying also leads to an increase in hardness (from 7.6±0.5 to 10.7±0.8 GPa) and elastic modulus (from 152±41 to 181±16 GPa).

The results of comparative tribological tests presented in Fig. 6, *b*, *c* and Table 3 prove that Mn introduction into the electrode significantly enhances the wear resistance of electrospark coatings, but hardly affects the coefficient of friction, the average value of

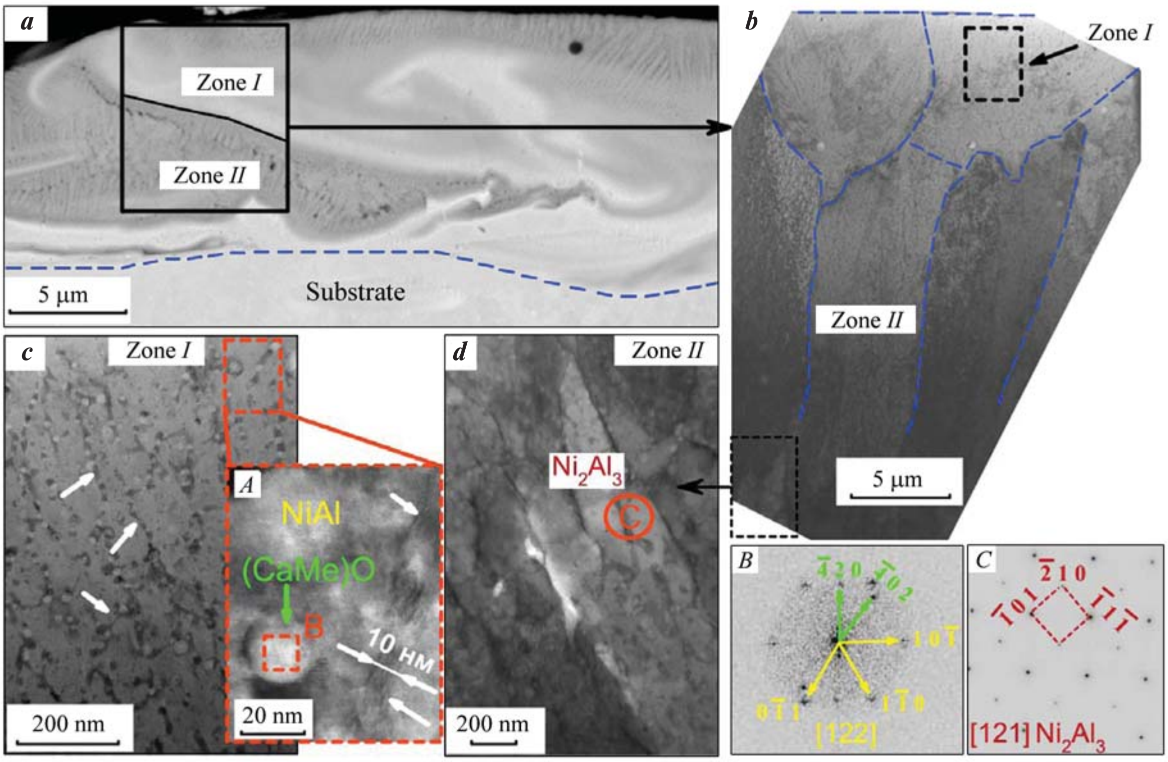

Fig. 4. Microstructure (***a***); TEM image of the lamella (***b***) and enlarged images of the corresponding coating zones (***c***, ***d***) formed by the Al–7Ca–1Mn electrode

A – HRTEM of (CaMe)O nanoparticles in the NiAl matrix; *B* and *C* – TEM diffraction patterns of the corresponding regions

Рис. 4. Микроструктура (***a***), ПЭМ-изображение ламели (***b***) и увеличенные изображения соответствующих зон покрытия (***c***, ***d***), сформированного электродом Al–7Ca–1Mn

A – ПЭМ ВР наночастиц (CaMe)O в NiAl-матрице; *B* и *C* – дифракционные картины ПЭМ соответствующих областей

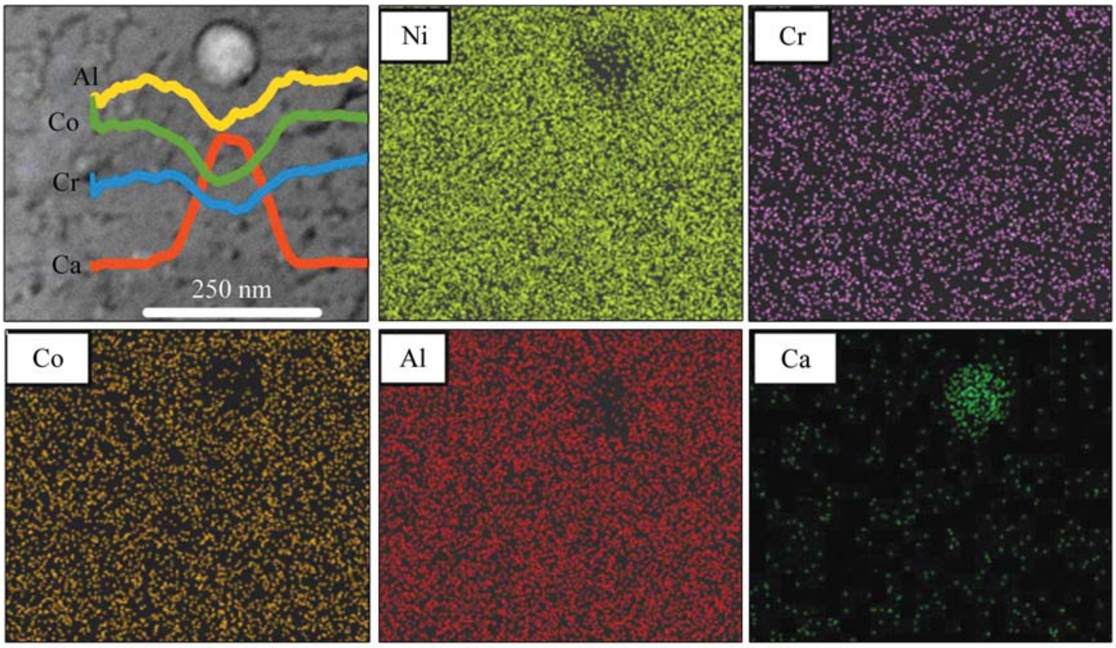

Fig. 5. TEM EDS spectra and the map of elemental distribution of (CaMe)O nanoparticle in the NiAl matrix

Рис. 5. ПЭМ ЭДС-спектры и карта распределения элементов наночастицы (CaMe)O в NiAl-матрице which correlates with the surface roughness. Its value was the lowest (0.27) when the electrospark coating was tested with minimal surface roughness (R_a = = 3.51±0.14 μm), which was formed during EST with the Al—7Ca—1Mn electrode with a thin eutectic structure (see Fig. 2, *d*).

Figure 6, *b*, *c* shows that wear resistance of samples subjected to EST significantly improves with an increase in the Mn content in the electrode from 0.5 to 1 at.% Mn. However, the increase in Mn concentration by more than 1 at.% does not result in a considerable surge of this indicator.

Figure 7 demonstrates the oxidation kinetic curves of the samples with electrospark coatings. We can see that EST enables to reduce the specific weight gain of EP741NP SLM alloy, which indicates a decreased oxidation rate. The kinetic curves of oxidation of the sample with 1.5 at.% Mn show a sharp increase in the mass after 10 h of isothermal curing. This is attributed to the violation of the oxidized coating integrity and unimpeded diffusion of oxygen into the substrate. The kinetic curves of oxidation of electrospark surfaces obtained during EST with Al—Ca—Mn electrodes, the Mn content amounting to 0, 0.5 and 1.0 at.%, present parabolic dependence [23; 24]:

$$(\Delta m/S)^n = kt, \tag{2}$$

where $\Delta m/S$ is the mass gain per unit area, mg/cm^2; k is the oxidation reaction rate constant; n is the oxidation reaction index; t is the oxidation time, h.

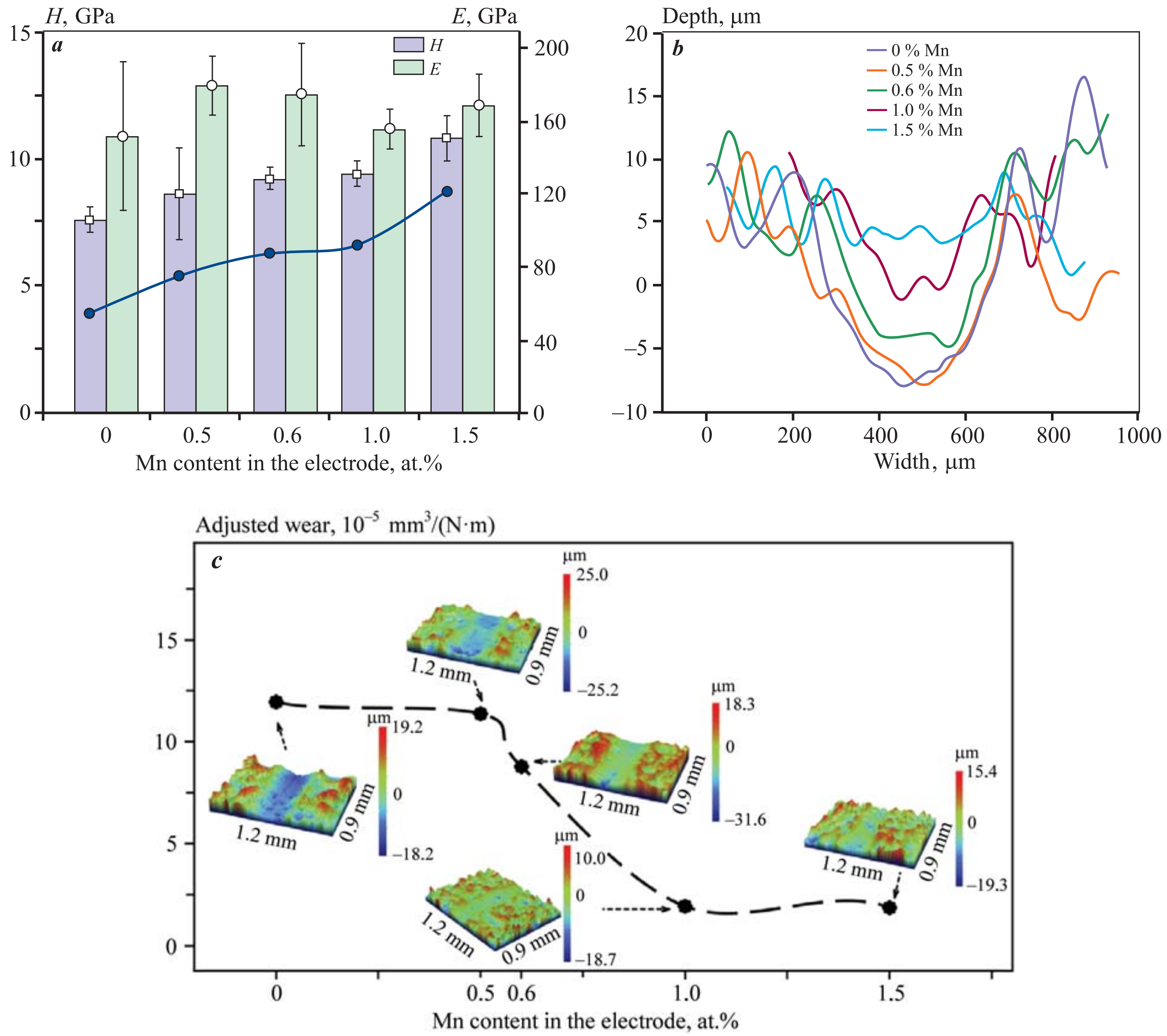

Fig. 6. Influence of the Mn content in the Al–Ca–Mn electrode composition on mechanical (***a***) and tribological (***b***, ***c***) properties of electrospark coatings

Рис. 6. Влияние содержания Mn в составе Al–Ca–Mn-электрода на механические (***a***) и трибологические (***b***, ***c***) свойства электроискровых покрытий

Table 3. **Tribological characteristics and surface roughness of samples with coatings obtained during EST with Al–Ca–Mn electrodes**

Таблица 3. Трибологические характеристики и шероховатость поверхности образцов с покрытиями, полученными при ЭИО электродами Al–Ca–Mn

Mn content in the electrode, at.%	Adjusted wear, 10^{-5} mm^3/(N·m)	Friction coefficient				R_a, μm
		Init.	Max.	Av.	Final	
0	11.95	0.27	0.45	0.29	0.28	4.38±0.57
0.5	11.37	0.15	0.46	0.30	0.27	4.33±0.17
0.6	8.78	0.07	0.52	0.31	0.31	4.87±0.87
1.0	1.93	0.09	0.40	0.27	0.28	3.51±0.14
1.5	1.86	0.37	0.47	0.29	0.28	4.04±0.15

To confirm the validity of the parabolic law of oxidation and to find the constants of equation (2), we used the approximation of oxidation curves, the results of which are presented in Table 4. The regression analysis of kinetic curves showed that treatment with electrodes, the Mn content ranging from 0 to 1.0 at.%, changes the oxidation mechanism from linear to parabolic. The analysis validity is confirmed by the values of the approximation coefficient which are close to unity: 0.9604—0.9846.

X-ray phase analysis was only performed on the samples which oxide layer was not destroyed during oxidation annealing (Table 5). Electrospark coatings subjected to isothermal oxidation annealing include the same phases. As the Mn content in the electrode increases, so does the proportion of calcium molybdate $CaMoO_4$ in them. However, the predominant phase in the surface layers of samples treated with electrodes without Mn and with 0.5 % Mn is Ni_3Al, whereas the oxidized layer of the coating obtained using an electrode with 1 % Mn is characterized by a large proportion of α-Al_2O_3 and $CaMoO_4$. This can be attributed to the smaller thickness of the oxide layers of the first two samples, which resulted in an increased relative intensity of the *X*-ray reflections from the substrate.

The surface layers of the above coatings also contain $NiAl_2O_4$ phases and insignificant amounts of NiO. The formation of $NiAl_2O_4$ spinel and the reduced share of α-Al_2O_3 on the surface of these samples can be put down to the interaction of aluminum oxide and nickel following the chemical reaction

$$NiO(т) + Al_2O_3(т) \rightarrow NiAl_2O_4(т). \qquad (3)$$

Figure 8 shows the microstructures of cross sections of coatings oxidized at t = 1000 °C during isothermal annealing for 30 h. The surface of all samples had a thin layer of variable thickness of 2.0—3.5 μm of tetragonal $CaMoO_4$ phase grains, the layer thickness not depending on the Mn content. Below is a layer of α-Al_2O_3, the thickness varying from 12.5 to 15.0 μm, in which $CaMoO_4$ regions are distributed, and light gray inclusions are found that have the following components, at.%: O — 71.1, Al — 8.0, Ti — 10.6, Nb — 4.6, Cr — 3.1, Ni — 1.4 and Co — 1.1.

Under the α-Al_2O_3 layer, in the heat affected zone of the substrate, an oxygen-free region consisting of γ'-Ni_3Al and β-NiAl is located, which is consistent with the XRD results. Beneath it, a band of white elongated precipitations is visible at a distance of 30—50 μm from the surface. EDS-analysis of fragments of this band showed an increased content of refractory elements, at.%: Co — 16.4, Cr — 14.9, Mo — 12.9 and W — 11.1. Such structures are characteristic of oxidized nickel alloys [25] and are called “topologically close packed” (TCP) phases.

It was not possible to correctly estimate the thickness of the oxide layer of the sample treated with an electrode with 1.5 % Mn due to its delamination (see inset *B* in Fig. 7). As a result of delamination, the thickness decreased (Fig. 8, *d*) and the integrity of the protective layer was violated causing unimpeded diffusion of oxygen deep into the nickel substrate, which is confirmed by the linear nature of oxidation (see Fig. 7). A distinctive feature of the initial electrospark coating (Fig. 8, *d*) formed with the electrode with 1.5 % Mn is a layered structure. As a result of the preferential grain boundary oxygen diffusion during annealing, fracture is registered at the interface boundaries between layers. The longitudinal crack along which the oxide layer delaminated is highlighted by blue arrows. According to the EDS data, delamination is most frequent in the regions with low aluminum content. This can probably be attributed to the low cohesion of the formed electrospark coating (see Fig. 3, *d*) due to its structural defects. Its distinctive feature is the increased the Mn content (up to 1.0 at.%), while in other samples it did not exceed 0.5 at.%.

Table 4. **Parameters of the equation of kinetic oxidation curves regression at 1000 °C temperature of the coatings formed by Al–Ca–Mn electrodes**

Таблица 4. Параметры уравнения регрессии кинетических кривых окисления при температуре 1000 °C покрытий, сформированных электродами Al–Ca–Mn

Mn content in the electrode, at.%	Time interval, h	Regression equation	Confidence coefficient of approximation	Oxidation rate, 10^{-4} mg/(cm^2·s)
Substrate (EP741NP)	$0 < \tau < 5$	$\Delta m/S = 0.278\tau^{0.5}$	0.9814	3.2
Substrate (EP741NP)	$5 \le \tau \le 30$	$\Delta m/S = 1.2176\tau - 1.8144$	0.9970	3.2
0	$0 \le \tau \le 30$	$\Delta m/S = 0.5022\tau^{0.5}$	0.9846	0.3
0.5	$0 \le \tau \le 30$	$\Delta m/S = 0.3803\tau^{0.5}$	0.9604	0.2
0.6	$0 \le \tau \le 30$	$\Delta m/S = 0.3863\tau^{0.5}$	0.9875	0.2
1.0	$0 < \tau \le 30$	$\Delta m/S = 0.5621\tau^{0.5}$	0.9805	0.3
1.5	$0 < \tau < 5$	$\Delta m/S = 0.4535\tau^{0.5}$	0.9506	3.1
1.5	$15 \le \tau \le 30$	$\Delta m/S = 0.278\tau^{0.5}$	0.9635	3.1

Table 5. **Phase composition of oxide layers of the coatings formed after 30 h of isothermal curing at $t = 1000$ °C in air**

Таблица 5. Фазовый состав оксидных слоев покрытий, сформированных после 30 ч изотермической выдержки при $t = 1000$ °C на воздухе

Mn content in the electrode, at.%	Phase	Structural type	Content, wt.%	Lattice period, nm	
				a	*c*
0	Ni_3Al	*cF*4/1	39.4	0.3582	–
	α-Al_2O_3	*hR*10/1	21.6	0.4779	1.3005
	$NiAl_2O_4$	*cF*56/2	18.9	0.8130	–
	$CaMoO_4$	*tI*24/16	15.3	0.5232	1.1427
	NiO	*cF*8/2	4.8	0.4184	–
0.5	Ni_3Al	*cF*4/1	34.8	0.3582	–
	α-Al_2O_3	*hR*10/1	20.9	0.4777	1.3019
	$CaMoO_4$	*tI*24/16	20.2	0.5230	1.1426
	$NiAl_2O_4$	*cF*56/2	18.3	0.8122	–
	NiO	*cF*8/2	5.8	0.4191	–
1.0	α-Al_2O_3	*hR*10/1	44.9	0.4752	1.2937
	$CaMoO_4$	*tI*24/16	43.3	0.5203	1.1382
	Ni_3Al	*cF*4/1	9.6	0.3585	–
	NiAl	*cP*2/1	2.2	0.2860	–

To thoroughly study the structure of oxide layers by the focused ion beam method, a lamella was cut from the cross section of the sample treated with the 1 % Mn electrode. Fig. 9 shows that the coating consisting of γ'- and β-phase grains with inclusions of spherical nanoparticles of (CaMe)O type was preserved under the oxide layer. In addition, at the grain boundaries there are conglomerates of particles, which, according to TEM data, are enriched with refractory elements, their composition corresponding to the formula $Ni_{23.4}Co_{21.7}Cr_{17}W_{16.2}Mo_{12.4}Al_{9.3}$.

The outer layer of the oxidized surface consists of large grains with interplanar distances (d_{101} = 0.48 nm; d_{224} = 0.15 nm), which corresponds to the scheelite-type $CaMoO_4$ phase with tetragonal crystal lattice $I4_1/a$ (Fig. 9, *e*). According to the works [26; 27], this structure exhibits excellent thermal stability and ultra-low thermal conductivity (0.6—1.2 W·m^{-1}·K^{-1}) at

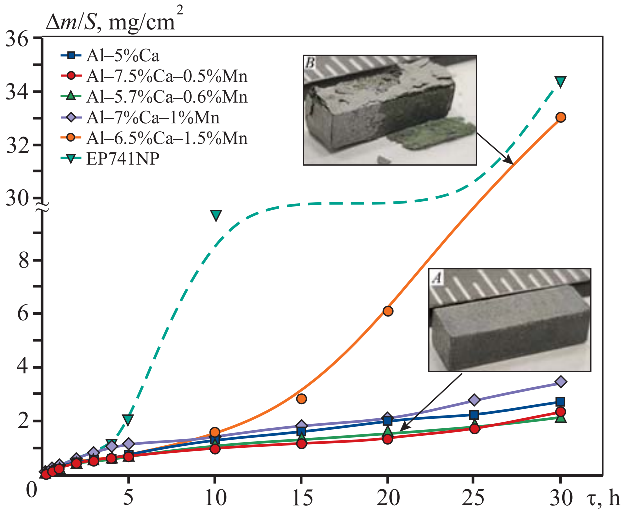

Fig. 7. Oxidation kinetic curves of the samples with coatings

The insets show the appearance of the samples obtained during EST with electrodes with 0.6 %Mn (*A*) and 1.5 % Mn (*B*)

Рис. 7. Кинетические кривые окисления образцов с покрытиями

На вставках показан внешний вид образцов, полученных при ЭИО электродами с 0,6 % Mn (*A*) и 1,5 % Mn (*B*)

$T = 400 \div 1000$ K, which is lower than that of thermal insulating layers for thermal barrier coatings such as YSZ ($1.5—3\ \mathrm{W \cdot m^{-1} \cdot K^{-1}}$).

The inner oxide layer in the sample subjected to EST with an electrode with 1 at.% Mn consists of equiaxed α-Al_2O_3 grains, about 400 nm in size. Nanoparticles up to 60 nm in size were found inside and at the periphery of the grains (Fig. 9, *b*, *d*). Based on the analysis of the HRTEM images, it can be assumed that they are nanoparticles of the Mn_2AlO_4 phase. The inset to Fig. 9, *d* shows the image of particles after Fourier transform. It can be seen that these particles with the $R\bar{3}m$ space group are coherent to the matrix of the α-Al_2O_3 ($R\bar{3}C$) oxide layer.

The delamination of the oxide layer of the sample treated with an electrode with 1.5 at.% Mn can be attributed either to the formation of particles in the matrix, in which the Mn content is higher than in the Mn_2AlO_4 phase, or to the supersaturation of this phase with manganese. The paper [28] confirms the first assumption. It shows that the presence of 1 at.% Mn in the electrode adversely affects the oxidation resistance of Ni—22Cr—14W—2Mo alloy as MnO particles form and reduce the strength of adhesion

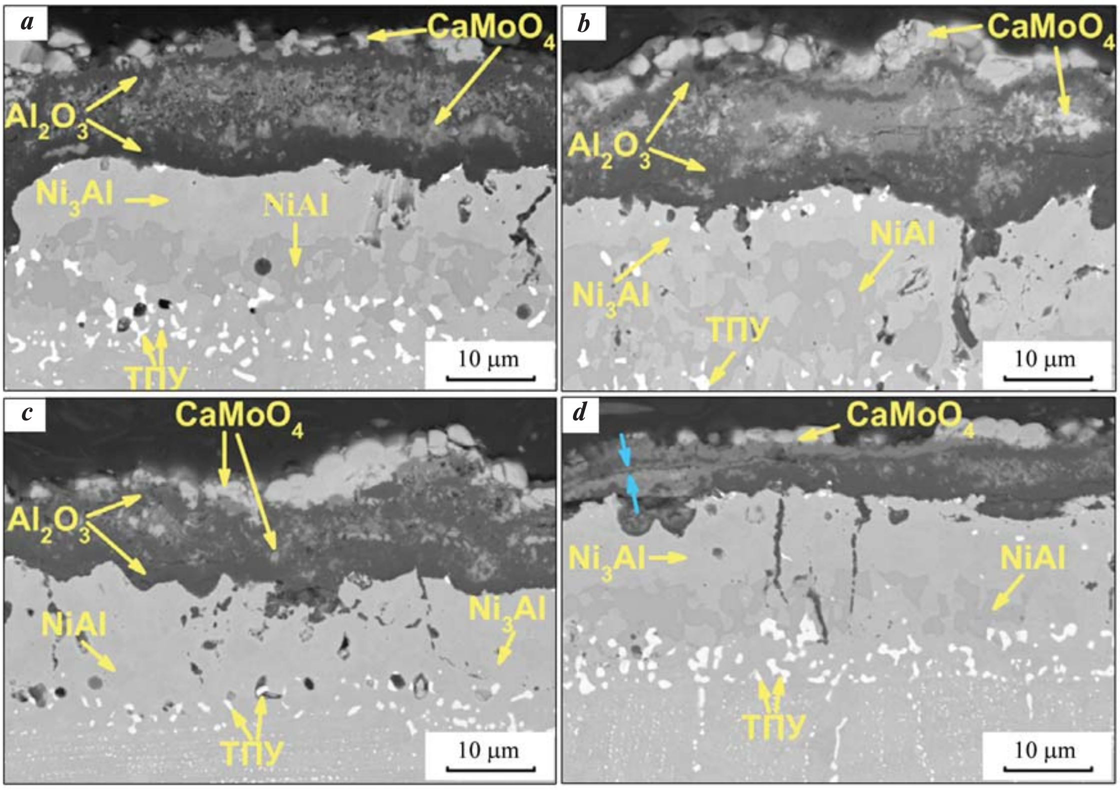

Fig. 8. SEM images of cross-sections of the samples with coatings obtained during EST with electrodes without Mn (***a***), and with the ones containing 0.5% Mn (***b***), 0.6% Mn (***c***), and 1.5% Mn (***d***), after 30 h of isothermal curing at *t* = 1000 °C

Рис. 8. РЭМ-изображения поперечных шлифов образцов с покрытиями, полученными при ЭИО электродами без Mn (***a***) и содержащими 0,5 % Mn (***b***), 0,6 % Mn (***c***) и 1,5 % Mn (***d***), после 30 ч изотермической выдержки при *t* = 1000 °C

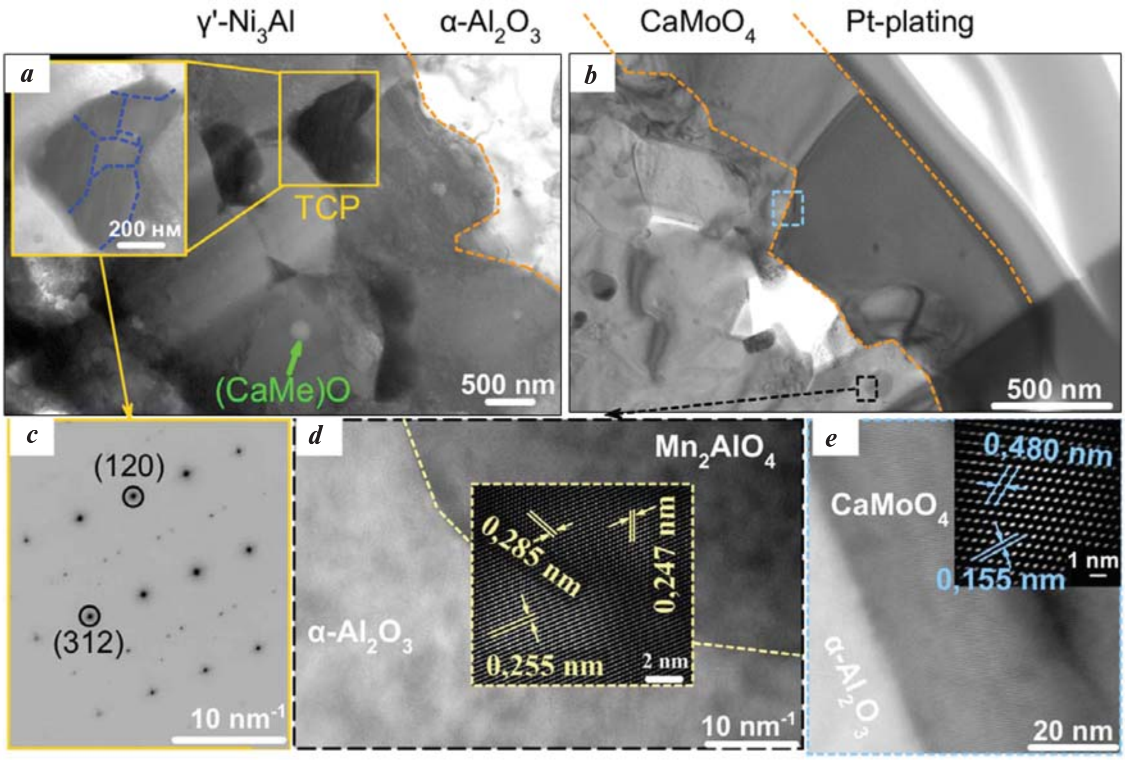

Fig. 9. TEM image of the structure of the 1 % Mn sample after 30 h of isothermal curing

a – boundary between the electrospark coating and α-Al_2O_3; ***b*** – boundary between oxide layers of α-Al_2O_3 and $CaMoO_4$;
c – diffraction pattern; ***d***, ***e*** – HRTEM of the corresponding regions

Рис. 9. ПЭМ-изображение структуры образца, обработанного электродом с 1 % Mn, после 30 ч изотермической выдержки

a – граница между электроискровым покрытием и α-Al_2O_3; ***b*** – граница между оксидными слоями α-Al_2O_3 и $CaMoO_4$;
c – дифракционная картина; ***d***, ***e*** – ПЭМ ВР-изображения соответствующих областей

between the Cr_2O_3 layer and the substrate. In the second case, manganese supersaturation of the Mn_2AlO_4 phase formed during annealing results in a change in the lattice parameter and accumulation of residual stresses at the interface [29] due to the dimensional mismatch between the crystal lattices of the phases causing loss of coherence and destruction of the oxide layer.

Conclusions

1. The study of mass transfer kinetics during electrospark treatment of SLM samples made of EP741NP alloy with electrodes with different Mn content showed that the highest substrate mass gain ($5.8 \cdot 10^{-4}$ g) was recorded when the near-eutectic Al—7%Ca—1%Mn alloy with a low degree of melt supercooling (Δt = 5 °C) was used. During EST with the Al—6.5%Ca—1.5%Mn electrode, structural defects are formed and the Mn concentration in the coating reaches 1.0 at.%. For the other studied coatings, it did not exceed 0.5 at.%.

2. The results of tests revealed that wear resistance, hardness and modulus of elasticity enhance with increasing manganese content in the coating. Increasing the mechanical properties start at manganese content of 0.5 at.% and its further growth up to 1.0 at.% leads also to a significant increase in wear resistance (adjusted wear of $1.86 \cdot 10^{-5}$ mm^3/(N·m)).

3. Electrospark treatment of EP741NP alloy with Al—Ca—Mn electrodes changes the oxidation kinetics from linear to parabolic. As the Mn content in the oxide layer increases, so does the volume fraction of calcium molybdate ($CaMoO_4$) in the oxidative annealing process. However, as the manganese content in the electrode reaches 1.5 at.%, oxidation proceeds by a mixed mechanism and is accompanied by violation of the oxide layer integrity and unimpeded diffusion of oxygen deep into the nickel substrate. This can probably be put down to MnO particles forming in the oxide matrix and reducing the bonding strength of the oxide layer. Another explanation is that residual stresses accumulate due to the mismatch of the phases crystal lattice parameters and coherence is lost between α-Al_2O_3 and Mn_2AlO_4 nanoscale particles supersaturated with manganese.

References

1. De Barbadillo J.J. 14-Inconel alloy 740H. (Ed. A.Di Gianfrancesco). In: *Materials for ultra-supercritical and advanced ultra-supercritical power plants.* Sawston, Cambridge: Woodhead Publ., 2017. P. 469—510. https://doi.org/10.1016/B978-0-08-100552-1.00014-2
2. Barella S., Boniardi M., Cincera S., Pellin P., Degive X., Gijbels S. Failure analysis of a third stage gas turbine blade. *Engineering Failure Analysis.* 2011;18(1):386—393. https://doi.org/10.1016/j.engfailanal.2010.09.017
3. Yang M., Zhou Y., Yang J., Bao J., Wang D., Yu Q. Performance analysis of an efficient waste heat utilization system in an ultra-supercritical coal-fired power plant. *Energy Reports.* 2022;8: 5871—720. https://doi.org/10.1016/j.egyr.2022.04.044
4. Peng J.Q., Zhang H.T., Li Y.F. Review of blade materials for IGT. *Procedia Engineering.* 2015;130:668—675. https://doi.org/10.1016/j.proeng.2015.12.295
5. Liang F., Meng A., Sun Y., Chen Zh., Jiang Zh., Zhang Y., Zhang Y., Zhu Y., Chen X. A novel wear-resistant Ni-based superalloy via high Cr-induced subsurface nanotwins and heterogeneous composite glaze layer at elevated temperatures. *Tribology International.* 2023;183:108383. https://doi.org/10.1016/j.triboint.2023.108383
6. Kamalan Kirubaharan A.M., Kuppusami P., Ghosh Ch., Priya R., Ningshen S., Dinesh Kumar D., Divakar R. Metal-ceramic diffusion barrier nanocomposite coatings on nickel based superalloys for corrosion and high temperature oxidation resistance. *Ceramics International.* 2022;48:31281—31288. https://doi.org/10.1016/j.ceramint.2022.06.203
7. Sanin V.V., Aheiev M.I., Kaplanskii Y.Y., Loginov P.A., Bychkova M.Y., Levashov E.A. The effect of dopants on structure formation and properties of cast SHS alloys based on nickel monoaluminide. *Materials.* 2023;16(9):3299. https://doi.org/10.3390/ma16093299
8. Kurzynowski T., Smolina I., Kobiela K., Kuźnicka B., Chlebus E. Wear and corrosion behaviour of Inconel 718 laser surface alloyed with rhenium. *Materials & Design.* 2017;132:349—359. https://doi.org/10.1016/j.matdes.2017.07.024
9. Behera A., Sahoo A.K. Wear behaviour of Ni based superalloy: A review. *Materials Today: Proceedings.* 2020;33(8):5638—5642. https://doi.org/10.1016/j.matpr.2020.04.007
10. Yu W., Ming W., An Q., Chen M. Cutting performance and wear mechanism of honeycomb ceramic tools in interrupted cutting of nickel-based superalloys. *Ceramics International.* 2021;47(13):18075—18083. https://doi.org/10.1016/j.ceramint.2021.03.123
11. Campos-Silva I., Contla-Pacheco A.D., Figueroa-López U., Martínez-Trinidad J., Garduño-Alva A., Ortega-Avilés M. Sliding wear resistance of nickel boride layers on an Inconel 718 superalloy. *Surface and Coatings Technology.* 2019;378:124862. https://doi.org/10.1016/j.surfcoat.2019.06.099
12. Yang Sh., Gao S., Xue W., Wu B., Cheng H., Duan D. Epitaxial growth and oxidation behavior of the NiCoCrAlYTa/Y_2O_3 coating on a nickel-based single—crystal superalloy blade tips, produced by electro spark deposition. *Journal of Alloys and Compounds.* 2023;931:167600. https://doi.org/10.1016/j.jallcom.2022.167600
13. Balaguru S., Gupta M. Hardfacing studies of Ni alloys: A critical review. *Journal of Materials Research and Technology.* 2021;10:1210—1242. https://doi.org/10.1016/j.jmrt.2020.12.026
14. Jude S.A.A., Winowlin Jappes J.T., Adamkhan M. Thermal barrier coatings for high-temperature application on superalloy substrates — A review. *Materials Today: Proceedings.* 2022;60:1670—1675. https://doi.org/10.1016/j.matpr.2021.12.223
15. Darolia R. Thermal barrier coatings technology: Critical review, progress update, remaining challenges and prospects. *International Materials Reviews.* 2013;58(6):315—348. https://doi.org/10.1179/1743280413Y.0000000019
16. Jayalakshmi V., Subramanian K.R.V. Thermal barrier coatings: state-of-art developments and challenges: A mini review. *Transactions of the IMF.* 2022;100(1):6—9. https://doi.org/10.1080/00202967.2021.1979813
17. Evans A.G., Clarke D.R., Levi C.G. The influence of oxides on the performance of advanced gas turbines. *Journal of the European Ceramic Society.* 2008;28(7):1405—1419. https://doi.org/10.1016/j.jeurceramsoc.2007.12.023
18. Mukanov S.K., Baskov F.A., Petrzhik M.I., Levashov E.A. Electro-spark treatment with low-melting Al—Si and Al—Ca electrodes in order to improve wear and oxidation resistance of EP741NP alloy prepared by selective laser melting. *Metallurgist.* 2022;66(3-4):317—326. https://doi.org/10.1007/s11015-022-01331-0
    Муканов С.К., Басков Ф.А., Петржик М.И., Левашов Е.А. Электроискровая обработка легкоплавкими электродами Al—Si и Al—Ca для повышения стойкости к износу и окислению сплава ЭП741НП, полученного селективным лазерным сплавлением. *Металлург.* 2022;3:70—77.
19. Junwei Fu, Kai Cui Effect of Mn content on the microstructure and corrosion resistance of Al—Cu—Mg—Mn alloys. *Journal of Alloys and Compounds.* 2022;896:162903. https://doi.org/10.1016/j.jallcom.2021.162903
20. Naumova E., Doroshenko V., Barykin M., Sviridova T., Lyasnikova A., Shurkin P. Hypereutectic Al—Ca—Mn—

(Ni) alloys as natural eutectic composites. *Metals.* 2021;11:890. https://doi.org/10.3390/met11060890

21. Petrzhik M., Molokanov V., Levashov E. On conditions of bulk and surface glass formation of metallic alloys. *Journal of Alloys and Compounds.* 2017;707:68—72. https://doi.org/10.1016/j.jallcom.2016.12.293
22. Arroyo-de Dompablo E., Ponrouch A., Johansson P., Palacín R. Achievements, challenges, and prospects of calcium batteries. *Chemical Reviews.* 2020;120(14):6331—6357. https://doi.org/10.1021/acs.chemrev.9b00339
23. Potanin A.Yu., Astapov A.N., Pogozhev Yu.S., Rupasov S.I., Shvyndina N.V., Klechkovskaya V.V., Levashov E.A., Timofeev I.A., Timofeev A.N. Oxidation of HfB_2—SiC ceramics under static and dynamic conditions. *Journal of the European Ceramic Society.* 2021;41(16): 34—47. https://doi.org/10.1016/j.jeurceramsoc.2021.09.018
24. Tian Sh., He A., Liu J., Zhang Y., Yang Y., Zhang Y., Jiang H. Oxidation resistance of TiAl alloy improved by hot-pack rolling and cyclic heat treatment. *Materials Characterization.* 2021;178:111196. https://doi.org/10.1016/j.matchar.2021.111196
25. Zhou B., He J., Liu L., Wang S., Sun J., Wei L., Guo H. The interaction between Dy, Pt and Mo during the short—time oxidation of (γ' + β) two-phase Ni—Al coating on single crystal superalloy with high Mo content. *Surface and Coatings Technology.* 2022;430:127999. https://doi.org/10.1016/j.surfcoat.2021.127999
26. Bsaibess E., Delorme F., Monot-Laffez I., Giovannelli F. Ultra-low thermal conductivity in scheelite and A-deficient scheelite ceramics. *Scripta Materialia.* 2021;201:113950. https://doi.org/10.1016/j.scriptamat.2021.113950
27. Ait Laasri H., Bsaibess E., Delorme F., Nataf G.F., Giovannelli F. Ultra-low lattice thermal conductivity in tungsten-based scheelite ceramics. *Journal of Alloys and Compounds.* 2023;955:170167. https://doi.org/10.1016/j.jallcom.2023.170167
28. Yun D. W., Seo S.M., Jeong H.W., Yoo Y.S. The effects of the minor alloying elements Al, Si and Mn on the cyclic oxidation of Ni—Cr—W—Mo alloys. *Corrosion Science.* 2014;83:176—188. https://doi.org/10.1016/j.corsci.2014.02.015
29. Zhou B., He J., Peng H., Sun J., Guo H. The influence of Hf content on oxide scale microstructure and HfO_2 formation mechanisms in two-phase (γ' + β) Ni—Al alloys. *Materials Characterization.* 2022;184:111659. https://doi.org/10.1016/j.matchar.2021.111659

Information about the authors

Samat K. Mukanov – Cand. Sci. (Eng.), Junior Research Scientist of the Laboratory “In situ Diagnostics of Structural Transformations” of Scientific Educational Center of Self–Propagating High-Temperature Synthesis (SHS-Center) of MISIS–ISMAN, National University of Science and Technology “MISIS” (NUST MISIS).
https://orcid.org/0000-0001-6719-6237
E-mail: smukanov@misis.ru

Mikhail I. Petrzhik – Dr. Sci. (Eng.), Professor of the Department of Powder Metallurgy and Functional Coatings (PM&FC) of NUST MISIS; Leading Research Scientist of the Laboratory “In situ Diagnostics of Structural Transformations” of SHS-Center of MISIS–ISMAN.
https://orcid.org/0000-0002-1736-8050
E-mail: petrzhik@shs.misis.ru

Pavel A. Loginov – Cand. Sci. (Eng.), Senior Lecturer of the Department of PM&FC of NUST MISIS; Senior Research Scientist of the Laboratory “In situ Diagnostics of Structural Transformations” of SHS-Center of MISIS–ISMAN.
https://orcid.org/0000-0003-2505-2918
E-mail: pavel.loginov.misis@list.ru

Evgeny A. Levashov – Dr. Sci. (Eng.), Prof., Academic of the Russian Academy of Natural Science, Head of the Department of PM&FC of NUST MISIS, Head of SHS-Center of MISIS–ISMAN.
https://orcid.org/0000-0002-0623-0013
E-mail: levashov@shs.misis.ru

Информация об авторах

Самат Куандыкович Муканов – к.т.н., мл. науч. сотрудник лаборатории «In situ диагностика структурных превращений» Научно-учебного центра (НУЦ) СВС МИСИС–ИСМАН, Национальный исследовательский технологический университет «МИСИС» (НИТУ МИСИС).
https://orcid.org/0000-0001-6719-6237
E-mail: smukanov@misis.ru

Михаил Иванович Петржик – д.т.н., профессор кафедры порошковой металлургии и функциональных покрытий (ПМиФП) НИТУ МИСИС; вед. науч. сотрудник лаборатории «In situ диагностика структурных превращений» НУЦ СВС МИСИС–ИСМАН.
https://orcid.org/0000-0002-1736-8050
E-mail: petrzhik@shs.misis.ru

Павел Александрович Логинов – к.т.н., ст. преподаватель кафедры ПМиФП НИТУ МИСИС; ст. науч. сотрудник лаборатории «In situ диагностика структурных превращений» НУЦ СВС МИСИС–ИСМАН.
https://orcid.org/0000-0003-2505-2918
E-mail: pavel.loginov.misis@list.ru

Евгений Александрович Левашов – д.т.н., акад. РАЕН, профессор, зав. кафедрой ПМиФП НИТУ МИСИС; директор НУЦ СВС МИСИС–ИСМАН.
https://orcid.org/0000-0002-0623-0013
E-mail: levashov@shs.misis.ru

Contribution of the authors

S.K. Mukanov – preparation and conduct of experiments, writing the text of the article, data analysis, visualization, discussion of the results.

M.I. Petrzhik – setting the purpose and objectives of the study, mechanical property research, data analysis, correcting the text, formulating conclusions.

P.A. Loginov – conducting transmission electron microscopy studies and discussing the results.

E.A. Levashov – forming the main concept, adjusting the text and conclusions.

Вклад авторов

С.К. Муканов – подготовка и проведение экспериментов, написание текста статьи, анализ данных, визуализация, обсуждение результатов.

М.И. Петржик – постановка цели и задачи исследования, исследование механических свойств, анализ данных, корректировка текста, формулировка выводов.

П.А. Логинов – проведение исследований методом просвечивающей электронной микроскопии, обсуждение результатов.

Е.А. Левашов – формирование основной концепции, корректировка текста и выводов.

The article was submitted 26.03.2024, revised 22.04.2024, accepted for publication 26.04.2024

Статья поступила в редакцию 26.03.2024, доработана 22.04.2024, подписана в печать 26.04.2024